Atmósfera 34(1), 1-23 (2021)
https://doi.org/10.20937/ATM.52747

Thermodynamic simulation of the seasonal cycle of temperature, pressure and ice caps on Mars

Víctor M. MENDOZA[1]*, Blanca MENDOZA[1,2], René GARDUÑO[1], Guadalupe CORDERO[3], Marni PAZOS[1], Sandro CERVANTES[4] and Karina CERVANTES[5]

[1]*Centro de Ciencias de la Atmósfera, Universidad Nacional Autónoma de México, Ciudad Universitaria, 04510 Ciudad de México, México.*
[2]*Escuela Nacional de Ciencias de la Tierra, Universidad Nacional Autónoma de México, Ciudad Universitaria, 04510 Ciudad de México, México.*
[3]*Instituto de Geofísica, Universidad Nacional Autónoma de México, Ciudad Universitaria, 04510 Ciudad de México, México.*
[4]*Posgrado en Ciencias de la Tierra, Universidad Nacional Autónoma de México, Ciudad Universitaria, 04510 Ciudad de México, México.*
[5]*Facultad de Ciencias, Universidad Nacional Autónoma de México, Ciudad Universitaria, 04510 Ciudad de México, México.*
*Corresponding author; e-mail: victor@atmosfera.unam.mx

Received: July 25, 2019; accepted: February 17, 2020

RESUMEN

Se presenta un modelo termodinámico para simular la temperatura y presión atmosféricas de Marte, la temperatura del regolito y el espesor vertical de los casquetes polares de CO_2 y su extensión horizontal. Esto se hace usando las temperaturas de la atmósfera y el regolito para cada día marciano del año, determinado a partir de la ecuación termodinámica. Suponiendo una atmósfera de CO_2, se calcula su espectro de emisión usando el calculador espectral E-Trans con la base de datos HITRAN (E-TRANS/HITRAN), lo que da como resultado una banda de 15 μm y el resto transparente, a través del cual la radiación emitida por el regolito y los casquetes de hielo (considerados como cuerpos negros) se escapa hacia espacio. También se incluye la extinción de la radiación solar por polvo atmosférico y su emisión de onda larga. La ecuación establece el equilibrio de energía entre la radiación solar absorbida y la radiación de onda larga saliente, incorporando también el calor latente liberado por la condensación de CO_2, el flujo de calor sensible desde la superficie a la atmósfera, el flujo de calor latente debido a la sublimación de hielo de CO_2 e intercambio de calor entre la capa de regolito superficial y sus capas inferiores, y el transporte de calor turbulento horizontal a escala planetaria atmosférica con un coeficiente de intercambio que es un orden de magnitud menor que el empleado en la troposfera terrestre. Considerando un promedio a largo plazo, el perfil vertical de temperatura del regolito se encuentra explícitamente utilizando la inercia térmica, incluida la conductividad; su regulación de temperatura se logra a través de la conducción térmica desde la superficie durante la estación cálida, y esta energía almacenada vuelve a la superficie durante la estación fría. Nuestro modelo simula la variación estacional de los casquetes polares y, en consecuencia, de la presión atmosférica superficial, a través del balance de masa de CO_2 entre ellos. Finalmente, se muestra explícitamente que la amplitud del ciclo de presión global estacional está modulada por un efecto termo-orográfico local, que aumenta (disminuye) esta amplitud en las regiones bajas (altas), y concuerda con las observaciones de los Viking Landers 1 y 2, y la Base de Datos Climáticos de Marte. Nuestra predicción para Hellas Planitia da un factor de amplificación de hasta 2.15, en coincidencia con otros autores.

ABSTRACT

We present a thermodynamic model to simulate the atmospheric temperature and pressure, the regolith temperature and the polar CO_2 ice caps vertical thickness and horizontal extent of Mars. This is done using the temperatures of the atmosphere and regolith for each Martian day of the year, determined from the thermodynamic equation. Assuming a CO_2 atmosphere, we calculate its emission spectrum using the spectral calculator E-Trans with the HITRAN database (E-Trans/HITRAN), resulting in only a band at 15 mm and the rest transparent, through which the radiation emitted by the regolith and ice caps (considered as black bodies) goes toward space. We also include the solar radiation extinction and longwave emission of atmospheric dust. The equation calculates the energy balance between the absorbed solar radiation and the outgoing longwave radiation, incorporating also the latent heat released by CO_2 condensation, the sensible heat flux from the surface to the atmosphere, the latent heat flux due to the CO_2 ice sublimation and the heat exchange between the surface regolith layer and its lower layers. The atmospheric planetary scale horizontal turbulent heat transport is parameterized with an exchange coefficient, which is an order of magnitude smaller than that employed in the terrestrial troposphere. Considering a long-time average, the regolith vertical temperature profile is explicitly found using the thermal inertia including conductivity; its temperature regulation is achieved through the thermal conduction from the surface during the warm season. This stored energy goes back to the surface during the cold season. Our model simulates the seasonal variation of the polar ice caps and consequently of the surface atmospheric pressure through the CO_2 mass balance between them. Finally, it is explicitly shown that the amplitude of the global seasonal pressure cycle is modulated by a local thermal-orographic effect, which increases (decreases) this amplitude in the low (high) regions, which agrees with the observations of the Viking Landers 1 and 2, and the Mars Climate Data Base. Our prediction for Hellas Planitia gives an amplification factor of up to 2.15, coinciding with other authors.

Keywords: Mars, thermodynamic simulation, CO_2 ice-polar cap, seasonal climate cycle.

1. Background

The Mars climate has undergone constant changes in the past. Studying the physical processes involved in such changes is a very challenging task and it will provide a better understanding of the present climate and its future tendency, not only of Mars but also of Earth (Fanale and Jakosky, 1982; McKay, 1999). A physical-mathematical simulation of the climate of Mars could seem less complicated than the simulations of the Earth's climate, because Mars nowadays lacks oceans, and the small amount of atmospheric water vapor (Spinrad et al. 1963), water ice clouds (Read and Lewis, 2004) and surface frozen water does not allow the existence of a vigorous hydrological cycle. However, simulations of the Martian climate can be complicated by the inclusion of thermodynamic and dynamic processes. One example is the storage of thermal energy in the lower layers of the regolith, which is a thermodynamic process that takes place by the conduction of heat from the surface during the warm season (boreal summer for Northern Hemisphere or boreal winter in the case of the Southern Hemisphere). This energy is returned to the atmosphere during the cold season (boreal winter for Northern Hemisphere or boreal summer in the case of the Southern Hemisphere) by conduction of heat from the lower layers to the surface. During the polar night, this flow of heat to the surface can regulate the growth of the polar ice cap, formed by the condensation of atmospheric CO_2. Another example is the development and spread of an incipient dust layer into a major storm. This is a positive radiative-dynamical feedback process, where the vertical velocity of the air increases due to the increase in its heating as a result of the solar radiation absorbed by the extra dust and reemitted (as longwave radiation) to the air. In this process, near the ground, stronger converging winds would be generated, which in turn would increase the dust uplift, reinforcing the storm (Read and Lewis, 2004).

In the present paper we attempt to simulate some aspects of the climate of Mars using an energy balance model of intermediate complexity, the Thermodynamic Climate Model (TCM), already used for the Earth´s climate (Adem, 1982). In the TCM the thermodynamic equation is applied to the atmospheric layer and the surface layer of the regolith together with the thermal conductivity equation. In the atmosphere the meteorological cyclones and anticyclones that transport heat from the equator to the

poles, are considered as turbulence and are incorporated in the thermodynamic equation as a horizontal diffusion process using a constant exchange (*austausch*) coefficient. In this way, dynamic processes are subordinated to the thermodynamic ones. These equations govern the climate state and evolution in terms of atmosphere and regolith temperatures and atmospheric pressure.

The paper is organized in the following manner: first, we present the model's equations and basic aspects; second, we show the model solutions, followed by results and conclusions.

2. The model

The TCM is a one-layer model (the troposphere) that has been integrated only in the Northern Hemisphere (NH) between ~ 12º and 90º and has been used to simulate past (Adem, 1981a, b; Mendoza et al. 2010), present (Adem, 1982) and future (Mendoza et el., 2016) climate changes of the Earth, as well as for monthly and seasonal forecast of temperature and precipitation (Adem et al., 2000). The first version of the model was global but one-dimensional, with latitude and time as independent variables; this version was used to explain the zonally averaged seasonal temperature in the troposphere, the position and intensity of the tropospheric jet and to formulate a method for seasonal forecast based on the storage of thermal energy in the ocean (Adem, 1963). In the present work, for the first time, we use a global two-dimensional version of the model to simulate the climate of Mars. In the model, the superscripts (*) and (′) indicate, respectively, that the variable is a function of height z, or that the variable is a perturbation with respect to a constant reference value (denoted with sub index 0) that is << than such value. In other words, all variables are functions of latitude φ, longitude ψ, height z measured from the surface and time t. The variables of the model (atmospheric temperature, regolith temperature and atmospheric pressure) correspond to mean daily climatic variables. The main forcing of the model is the mean daily insolation, which changes from sol to sol throughout the Martian year. In the present work we will use the term sol, when referring to the Martian day.

Compared to other climate models, the TCM has basically two advantages: (*a*) physical processes are modeled with intermediate complexity and therefore are easily understandable, and (*b*) the dynamics is subordinated to thermodynamics, which implies fewer computing resources. So, many simulations can be performed in much less time than for most other climate models that explicitly reproduce dynamics.

2.1 Temperature, pressure, and density

The model considers an atmospheric layer of thickness H with a constant lapse rate Γ. The absolute temperature T^* is:

$$T^* = \Gamma[H(\varphi,\psi,t) - z] + T(\psi,\varphi,t) \tag{1}$$

where T (ψ, φ, t) is the temperature at $Z = H$. We assumed that for $z > H$ the absorption and emission of atmospheric gases is negligible, thus $z = H$ is the radiation boundary of the model. The lapse rate measurements showed temperature profiles that are non-linear functions of the height. Five entry temperature-pressure profiles from Viking Lander 1 (VL1), Viking Lander 2 (VL2), Mars Pathfinder, Spirit and Opportunity are reported by Withers and Smith (2006). For instance, the Spirit profile can be represented by a relatively smooth quadratic curve in a layer between 30 and 80 km, but between 5 and 30 km can be approximated by an isothermal layer. Opportunity showed three thermal inversions between ~ 6 and 80 km, the first one between ~ 8 and 12 km, the second one between ~ 22 and 24 km, and the third one between ~ 56 and 64 km. However, to a first approximation the five profiles can be represented up to ~ 55 km by a lapse rate of $\Gamma = 1.23\ K\ \mathrm{km}^{-1}$.

The atmospheric pressure p^* and density ϱ^* are obtained assuming the hydrostatic equilibrium and the ideal gas equations:

$$p^* = p\left(\frac{T^*}{T}\right)^{g/R\Gamma} \tag{2}$$

$$\rho^* = \rho\left(\frac{T^*}{T}\right)^{\frac{g}{R\Gamma}-1} \tag{3}$$

where $g = 3.72\ \mathrm{ms}^{-2}$ is the gravity acceleration at the surface, $R = 192\ JKg^{-1}\ K^{-1}$ is the gas constant (Read and Lewis, 2004), $p = (p^*)_{z=H}$ and $\varrho = (\varrho^*)_{z=H}$. We also assume that H is constant, and T (at this level) is variable:

$$H=H_0$$
$$T=T_0+T' \tag{4}$$

If H_s (φ,ψ) is the orographic height relative to the planet´s reference pressure level of ~ 6.4 mb at $z = 0$ (Smith et al., 1999a), the vertically averaged temperature is:

$$T_m = \frac{1}{(H-H_s)}\int_{H_s}^{H} T^*\, dz \tag{5}$$

2.2 The model equations

The temperature T_m (φ,ψ,t) is governed by the thermodynamic equation integrated in the atmospheric layer of thickness $H - H_s$. This equation is two-dimensional and has a mathematical structure similar to the one-dimensional equation of the first global version of the TCM (Adem, 1963); that is, it is a linear elliptic differential equation of the second degree, which can be expressed as:

$$\underbrace{c_1 \frac{\partial T'_m}{\partial t}}_{ST} - \underbrace{c_3 K\left[\frac{\partial^2 T'_m}{\partial \varphi^2} - \tan\varphi \frac{\partial T'_m}{\partial \varphi} + \frac{1}{cos^2\varphi}\frac{\partial^2 T'_m}{\partial \psi^2}\right]}_{TU} = E_T + G_2 + G_5 \tag{6}$$

where $T_m = T_{m_0} + T'_m$, $c_1 = c_V \rho_m (H - H_s)$ and $c_3 = c_1/r_0^2$; $c_V = 652.8\ Jkg^{-1}\ K^{-1}$ is the specific heat at constant volume, $r_0 = 3389.5$ km is the Mars radius (Read and Lewis, 2004) and ρ_m is the layer average density given by:

$$\varrho_m = \frac{1}{(H-H_s)}\int_{H_s}^{H} \varrho^*\, dz \tag{7}$$

Using (2) and (3) in (7):

$$\varrho_m = \frac{p}{g(H-H_s)}\left[\left(\frac{T_s}{T}\right)^{\frac{g}{R\Gamma}} - 1\right] \tag{8}$$

where T_s is the temperature at $z = H_s$.

In (6) the left-hand side term ST represents the layer's storage of thermal energy, and the TU term the planetary horizontal turbulent transport of thermal energy, parameterized through an exchange coefficient K. On the right side E_T, G_2 and G_5 are, respectively, the fluxes of shortwave and longwave net radiation, the vertical turbulent sensible heat flux from the surface, and the release of latent heat by the CO_2 condensation.

We assumed that the upper surface regolith layer has a thickness h_r, density ϱ_r, specific heat c_r and temperature T_r. The energy equation of this layer is:

$$\underbrace{h_r \varrho_r c_r \frac{\partial T'_r}{\partial t}}_{ST_r} = E_r + G_1 - G_2 - G_3) \tag{9}$$

The left-hand side ST_r is the thermal energy per unit area column stored in the regolith layer, E_r is the shortwave and longwave net radiation, G_1 is the energy gained by the upper regolith layer by heat conduction from the lower layers, and G_3 is the surface thermal energy lost by the vertical turbulent latent heat flux by ice sublimation.

In the diurnal cycle, solar radiation absorbed in the day is stored in the regolith as thermal energy and released at night as heat. Considered a long-time average, we will have a similar process: during the warm Martian season, the solar radiation absorbed by the surface is transmitted by thermal conduction to the lower layers and stored as thermal energy. During the cold season this energy is conducted towards the surface where it is released as heat. In the polar regions this process has an important role in ice sublimation. Then the temperature T_r^* (at the surface) of each lower layer is ruled by the equation of thermal conductivity:

$$\rho_r c_r \frac{\partial T_r^*}{\partial t} = k_v \frac{\partial^2 T_r^*}{\partial z^2} \tag{10}$$

where k_v is the thermal conductivity coefficient, related to the thermal inertia (I_T) which is a function of the layer's density, specific heat and thermal conductivity (Piqueux and Christensen, 2011):

$$I_T = \sqrt{(\rho_r c_r k_r)} \tag{11}$$

2.3 Atmospheric radiation

Equation (2) can be expressed as a function of the surface temperature T_s and pressure p_s at $z = H_s$:

$$p^* = p_s\left(\frac{T^*}{T_s}\right)^{g/R\Gamma} \tag{12}$$

Here (1) is expressed in terms of T_s:

$$T^* = T_s - \Gamma\,(z - H_s) \tag{13}$$

The Mars atmosphere is mainly CO_2, therefore this gas is the main long-wave absorber of the atmosphere. The partial CO_2 density is:

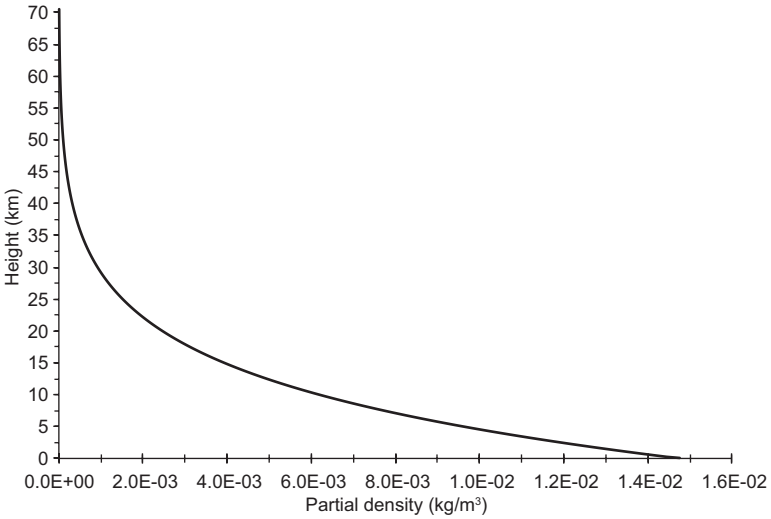

Fig. 1. CO_2 partial density of the Martian atmosphere as a function of height, calculated from Eqs. (12), (13) and (14), considering $T_s = 214.6$ K and $p_s = 6.4$ mb.

$$\rho^*_{CO_2} = \frac{M_{CO_2}}{M}\chi_{CO_2}\rho^* = r_c\rho^* = 0.96\frac{p^*}{RT^*} \tag{14}$$

Here M_{CO_2}=44.01 *g/mol*, χ_{CO_2}=0.95, M=43.34 *g/mol* (Franz et al., 2017) and $r_c = M_{CO_2}\chi_{CO_2}/M = 0.96$) which are the molecular ideal gas weight, the CO_2 molar fraction, the average molecular weight and the mixing ratio, respectively.

Figure 1 shows the partial CO_2 density as a function of height obtained from (14) and using (12) and (13) with characteristic surface values $T_s = 214.6$K and $p_s = 6.4$ mb. Using these temperature and pressure values and the lapse rate of $1.23K$ km^{-1}, the temperature-pressure profile reproduces well the average of the five entry profiles reported by Withers and Smith (2006) mentioned previously.

It is observed that above 55 km the CO_2 partial density is negligible. Then we assumed that $H = H_0 = 55$ km is an appropriate limit for the model upper radiation boundary, and above this level there are no emission gases. The gas mass (kg m^{-2}) in the unit column of height H is:

$$U_{CO_2} = \int_{H_s}^{H}\rho^*_{CO_2}\,dz = \int_{H_s}^{H} r_c\rho^*\,dz = \frac{0.96}{g}(p_s - p) \cong \frac{0.96}{g}p_s \tag{15}$$

In (15) we also used (14), the hydrostatic equilibrium equation and considered that $p/p_s << 1$.

The atmospheric emissivity has been found using the E-Trans/HITRAN (E-Trans is a commercial software available at http://www.jcdpublishing.com/about.html) with the HITRAN database version 2004 (Rothman et al., 2005). E-Trans/HITRAN was used successfully for the Earth atmosphere (Mendoza et al., 2017) and now is applied to the Mars atmosphere. When an atmospheric layer is non-isothermal (nor isobaric), E-Trans/HITRAN needs the equivalent temperature and pressure for each component. These variables are defined as the weighted averages with respect to the layer gas content. The CO_2 equivalent temperature and pressure are:

$$T_e = \frac{\int_0^U T^*\,dU_{CO_2}}{\int_0^U dU_{CO_2}} = \frac{\int_p^{ps} T^*\,dp^*}{\int_p^{ps} dp^*} = \frac{g}{g + R\Gamma}\bullet$$

$$\begin{vmatrix} \frac{g+R\Gamma}{g} & \frac{g+R\Gamma}{g} \\ p_s & -p \\ \frac{g+R\Gamma}{g} & \frac{g+R\Gamma}{g} \\ p_s & -pp_s \end{vmatrix} T_s \cong \left(\frac{g}{g+R\Gamma}\right)T_s = 0.941T_s \tag{16}$$

$$p_e = \frac{\int_0^U p^* \, dU_{CO_2}}{\int_0^U dU_{CO_2}} = \frac{\int_p^{ps} p^* \, dp^*}{\int_p^{ps} dp^*} = \frac{1}{2}\,(p_s - p) \cong \frac{1}{2}\,p_s \tag{17}$$

In (17) we used (15) and the hydrostatic equilibrium equation, and we assumed that $p/p_s << 1$. Using (14), (15) and (17), U_{CO_2} can be written as:

$$U_{CO_2} = \frac{r_c}{g}\,2p_e = \frac{0.96}{g}\,2p_e \tag{18}$$

The lowest equivalent gas pressure that can work with E-Trans/HITRAN is ~ 135 mb (~ 101 Torr). If the surface atmospheric average pressure is ~ 6.4 mb, then according to (17), p_e = 3.2 mb. However, we can increase artificially the equivalent gas pressure of the emission layer while keeping constant the gas mass U_{CO_2}, under the hypothesis that its emissivity depends basically on the number of molecules (optical path) in the layer, just as we did previously for the stratospheric layer of O_3 on Earth (Mendoza et al., 2017). Then, if U_{CO_2} is constant, (18) implies that:

$$r_c' \, p_e' = r_c \, p_e \tag{19}$$

Here $r_c = 0.96$ and $p_e = 3.2$ mb. Therefore, increasing the pressure to $p_e' = 135$ mb, we found $r_c' = 0.022$. The process of increasing artificially the pressure while decreasing the gas mixing ratio, can overestimate the layer's emissivity due to the widening. This is caused by the pressure increase and to a lesser degree by the temperature increase of the spectral lines (e.g., Kondratyev, 1969). This will be noted only in the edges of the 15 μm CO_2 band (constituted by many superposed lines). In this way, to not overestimate even more the emissivity of this band, we have taken this minimum pressure value (135 mb) with which E-Trans / HITRAN software can work. Figure 2 shows the CO_2 atmospheric emission spectrum modulated by the Planck curve at 214.6 K,

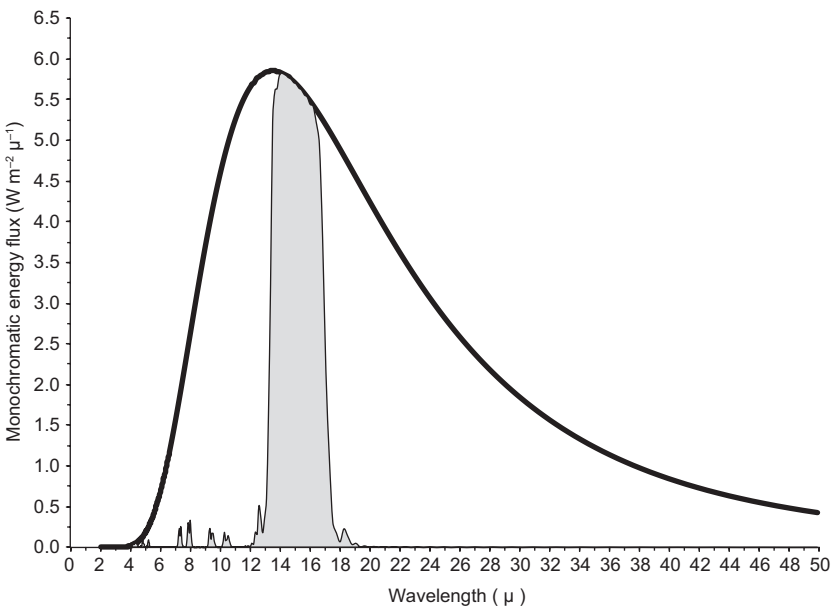

Fig. 2. Monochromatic energy flux ($Wm^{-2}\ \mu^{-1}$) from Planck's spectrum (thick line) and emission bands of the atmospheric CO_2 at the Martian surface for 214.6 K (gray area), obtained with E-Trans/HITRAN. We used an equivalent pressure of 135 mb and a mixing ratio of 22 700 ppm. The average width of 15 μm band is ~ 3.5 μ and its area with respect to the total area under the Planck curve is the emissivity $\epsilon_{CO_2} = 0.24$.

constructed with the equivalent temperature of 201.9 K, obtained from (16) with $T_S = 214.6$ K, and pressure increased to 135 mb but with the mixing ratio reduced to 22,700 ppm, instead of the typical conditions of 3.2 mb and 960,000 ppm. In Figure 2, the gray area with respect to the total area under the Planck curve is the emissivity, which is equal to 0.24

Atmospheric emission bands were obtained by the spectrometer IRIS on board of Mariner 9, close to 21º S in a relatively warm region at 280 K (Read and Lewis, 2004). The spectrometer´s average width of the main band of 15 μm is ~ 3.2 μm and the one obtained with E-Trans/HITRAN software is ~ 3.5 μm, which are similar. The emissivity calculated with E-Trans/HITRAN software in order to get a band of 3.2 μm is 0.22, which means that reducing the band width from 3.5 μm to 3.2 μm reduces the CO_2 emissivity by 8.5%. Then we can confidently use this spectral calculator for future experiments where the atmospheric mass is increased (for instance for models of the terraformation of Mars).

2.4 Daily insolation at the top of the atmosphere and at the surface

Using the Milankovitch (1920) expression with the orbital Martian parameters:

$$I = S_0 \left(\frac{a_0}{r}\right)^2 \cos Z \tag{20}$$

Here I is the instantaneous solar radiation (insolation) at the surface in the absence of an atmosphere, $S_0 = 590$ Wm^{-2} is the total solar irradiance, a_0 is the orbit´s major semiaxis, r is the instantaneous Sun-Mars distance and Z is the zenith angle given by:

$$\cos Z = \sin \varphi \sin \delta + \cos \varphi \cos \delta \cos \omega \tag{21}$$

where δ is the solar declination angle and ω is the hourly angle $\omega = 2\pi t/P$, with t the afternoon time and $P = 88{,}750$ s the duration of the sol. The angle δ depends on the obliquity $\eta = 25.2$º and the areocentric longitude (L_s) expressed in degrees such that 0º corresponds to the vernal equinox. All the seasons, solstices and equinoxes are named for the NH, so they should be understood as "boreal". The angles δ, η and L_s are related by:

$$\sin \delta = \sin \eta \quad \sin L_s \tag{22}$$

Substituting (21) in (20) and integrating along the sol, we found the average daily insolation (Adem, 1962):

$$I_d = \frac{S_0}{\pi} \left(\frac{a_0}{r}\right)^2 \bullet \\ [\omega_1 \ \sin \varphi \sin \delta + \sin \omega_1 \ \cos \varphi \cos \delta] \tag{23}$$

where ω_1 is the longitude at noon in radians:

$$\cos \omega_1 = -\tan \varphi \tan \delta \tag{24}$$

for the polar regions $\cos \omega_1 = -1$ and $\cos \omega_1 = 1$ at dusk and dawn, respectively, during times longer than one day.

The instantaneous Sun-Mars distance can be found from:

$$\left(\frac{a_0}{r}\right) = \frac{1 + e \cos (L_s - L_s^p)}{1 - e^2} \tag{25}$$

Here $e = 0.093$ is the orbit's eccentricity and $L_S^p = 248$º is the areocentric longitude at the perihelion (Appelbaum et al., 1993).

Since we are interested in the seasonal climate cycle, we determined the average daily temperatures of the atmosphere (T'_m) and of the regolith (T'_r). Then, in E_T and E_r of (6) and (9), respectively, we must use the average daily insolation given by (23) instead of the instantaneous insolation given by (20). Figure 3 shows the average daily insolation, indicating that during the boreal winter solstice the Southern Hemisphere (SH) gets much more radiation than the NH during the boreal summer solstice, unlike the Earth, where the difference is small. The reason is the Mars eccentricity, which is nowadays 5.6 times larger than that of our planet.

The atmosphere of Mars is practically transparent to visible radiation (Stephen, 2003), so that the solar radiation extinction through the atmosphere is mainly due to the suspended dust particles and water ice haze (Toigo and Richardson, 2000). The total solar radiation I_{Tot} that reaches the horizontal surface is the sum of the direct plus the diffuse radiations; the I_{Tot} is a fraction of I given by (20), which depends on the zenith angle Z and the optical thickness τ, that we attribute to the atmospheric suspended dust particles. A simplified model to calculate I_{Tot} is taken from Appelbaum et al. (1993):

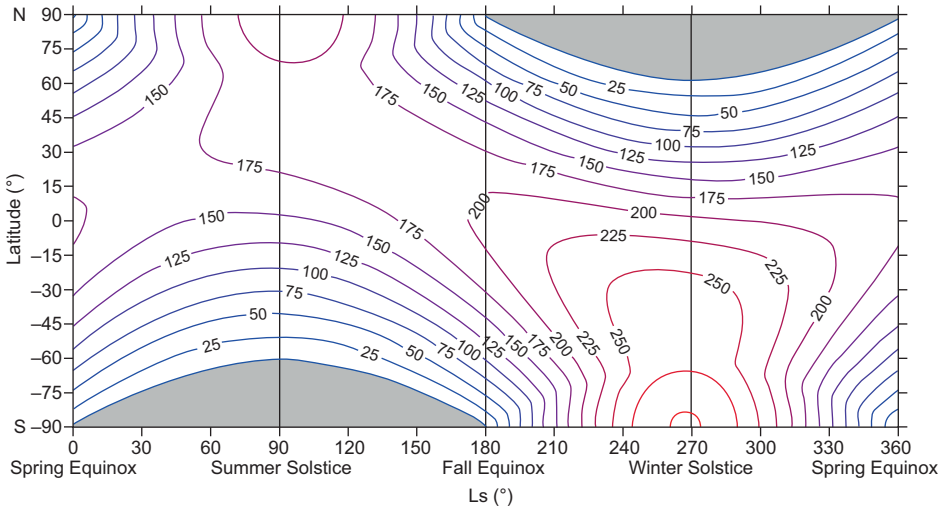

Fig. 3. Average daily solar insolation I_d at the top of the Martian atmosphere in Wm^{-2}, as a function of the latitude and areocentric longitude (L_s). The equinoxes (spring and autumn) and the solstices (summer and winter) correspond to L_s = 0º, 180º and L_s = 90º, 270º, respectively. The red contour corresponds to the largest value.

$$I_{Tot} = S_0 \left(\frac{a_0}{r}\right)^2 \cos Z \left(\frac{2\cos Z}{\tau + 2\cos Z}\right) \quad (26)$$

The Viking missions measured τ in two NH locations, a tropical (22.3º), and a mid-latitude (47.7º) region, finding that during relatively clear atmospheric conditions (spring and summer) τ showed values between 0.2 and 0.7, while during dust storm times (autumn and winter) τ reached values between 1.0 and 3.3 (Appelbaum et al., 1993). However, τ can acquire larger values. During the global dust storm on Mars in June 2018, Opportunity recorded the gradual darkening of the Sun from relatively large and bright to so obscured and small that it could just be perceived; the corresponding values of τ were from 1, for the brightest Sun, to 11, for the almost imperceptible Sun (http://www.nasa.gov/rovers and http://marsrovers.jpl.nasa.gov.).

To model these observations, with the dust storms removed, τ is (Stephen et al., 1999):

$$\tau = 0.7 + 0.3cos\,(L_s + 80º) \quad (27)$$

The equation for the direct solar radiation (I_D) can be found from the Beer Law, which estimates the light absorption due to dust particles (Appelbaum et al., 1993); it is a function of the optical thickness:

$$I_D = S_0 \left(\frac{a_0}{r}\right)^2 cos\, Z \exp\left(-\frac{\tau}{\cos Z}\right) \quad (28)$$

The diffuse solar radiation is just the difference between the I_{Tot} (26) and I_D (28).

Equations (26) and (28) are integrated over one sol using the Simpson's Rule. Figure 4 shows I_{Tot}, for a relatively clear atmosphere (τ = 0.4). Considering average daily values of τ and I_{Tot}, according to the Mars Climate Data Base (MCD) for L_S = 200º, 45º N and 120º E, it is found that τ = 0.40 and I_{Tot} = 87.6 Wm^{-2}. According to Figure 4, our result for L_S = 200º and 45º N with τ = 0.4 is I_{Tot} 85.0 Wm^{-2}, which suggests some agreement with the MCD.

2.5 The terms of storage and transport

To estimate the storage term *ST*, the first left hand side term of (6) ($c_1\, \partial T'_m/\partial t$), we find that for NH in middle desert latitudes, the factor $\partial T'_m/\partial t$ is almost of the same magnitude for Mars than for Earth (e.g., in the cold desert of Gobi): 30º and 20º C, respectively, for the winter-summer time span. To calculate the increase of T_m from winter to summer on Mars, we use the observed temperature profiles of the Mars Global Surveyor for 6 years (Hinson, 2008), taking temperature at the pressure level $P_s/2$ and at 45 ºN. In the case of Earth, we use the NCEP/NCAR

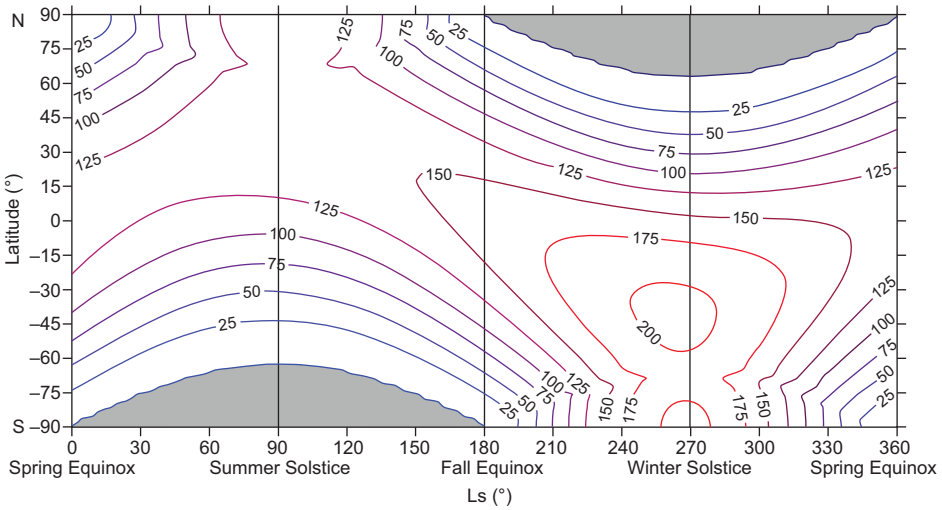

Fig. 4. As in Figure 3, but for the total daily solar radiation (Wm^{-2}) on the horizontal surface, calculated for the conditions of a relatively clear atmosphere with $\tau = 0.4$. The red contour corresponds to the largest value.

reanalysis data at 500 mb level over the Gobi Desert, for the 30-year period 1961-1990. We use the factor $c_1 = c_V \rho_m (H - H_s) \approx c_V \rho_m H = 1.06x10^{5}\ Jm^{-2}\ K^{-1}$ for the Martian atmosphere, while $c_V \rho_m H = 5.76x10^{6}$ $Jm–2\ K^{-1}$ for the Earth´s atmosphere, assuming an atmospheric terrestrial layer $H \sim 11$ km. This implies that the terrestrial ST value is ~ 36 times larger than the Mars value. We have also assumed a thickness of the regolith upper layer of $h_r = 0.02m$, then $\rho_r = 1.5\times10^{3}\ kgm^{-3}$ and $c_r = 0.837\times10^{3}\ J\,kg^{-1}\ K^{-1}$ (Fanale and Cannon, 1971), and $h_r\, \varrho_r\, c_r = 0.8x10^{5}\ Jm^{-2}\ K^{-1}$. For the Earth, the equivalent storage term ST_r can be negligible (Adem, 1964). Thus, it is reasonable to assume that for Mars, in (9) the storage term ST_r can also be negligible. However, we do not neglect the atmospheric storage term ST for Mars, since it can be important in terraforming experiments, where the mass of the atmosphere is increased due to the greenhouse gases.

Pollack et al. (1990) and Barnes et al. (1993) found that the meridional turbulent heat transport in Mars is important at a global scale. Their calculations showed that such transport around 60 ºN can contribute approximately 5 Wm^{-2} to the heat balance at those latitudes. On the Earth, meteorological cyclones and anticyclones at mid-latitudes are associated with turbulent horizontal heat transport from the equator to the poles (Adem, 1962). Those terrestrial cyclones and anticyclones obtain almost all of their energy from the baroclinic conversion of the zonal flux, but in Mars this conversion has both a baroclinic and a barotropic character (Holopainen, 1983). In (6), the meridional component of the horizontal turbulent transport (TU), comes from the divergence of the following parameterization:

$$\overline{v^{*\prime\prime} T^{*\prime\prime}} = -K \quad \frac{1}{r_0} \frac{\partial \overline{T}^{*}}{\partial \varphi} \tag{29}$$

where $v^{*\prime\prime}$ is the meridional component of the turbulent or eddy velocity and $T^{*\prime\prime}$ is the temperature perturbation field; the upper bar means an average over a sufficiently long time such that $\overline{v^{*\prime\prime}} = 0$ and $\overline{T^{*\prime\prime}} = 0$. The process given by (29) can be described as follows: the insolation gradient from the equator to the pole, mainly in mid-latitudes and during winter, produces a meridional temperature gradient represented on the right side of (29); as a response, a turbulent horizontal flow of heat against gradient is established, given by the eddy covariance on the left side of (29). The effect of the divergence of this turbulent flow, the TU term of (6), is to reduce the meridional temperature gradient.

In the terrestrial atmosphere, the parameterization expressed by (29), is satisfied using an *austaush* coefficient $K \approx 5\times10^{6}\ m^2\ s^{-1}$ (Stewart, 1945; Adem, 1962). Typical Martian values for the eddy covariance

$\overline{v^{*\prime}T^{*\prime}}$ in a month close to the winter solstice at ~20 km (~ the middle atmosphere of our model, $z = (H - H_s)/2$), are 10, –2.5 and –0.2 ms^{-1} K, for latitude ranges of 50º to 70º N, 10º to 40º N and 10º to 70º N, respectively (Barnes et al., 1993). The corresponding temperature gradients $\partial\overline{T^*}/\partial(r_0\,\varphi)$ obtained from http://www-mars.lmd.jussieu.fr/mars/access.html, are -2.54×10^{-5}, 5.63×10^{-6} and 7.04×10^{-7} K km^{-1}. Using these values and (29) we found an average coefficient $K \approx 3.7\times10^5$ m^2 s^{-1} for the Martian atmosphere, which is one order of magnitude smaller than the terrestrial one. Defant (1921) was the first to consider cyclones and anticyclones of planetary scale as turbulent eddies. He found that the *austausch* coefficient depends on the size of these eddies. On Mars, whose surface is 0.28 of the Earth's surface, the eddies of planetary scale must have a smaller size than those of the Earth (approximately in the same proportion of 0.28). Therefore, the exchange coefficient we have found for Mars is consistent with Defant's ideas.

2.6 Heating functions

The heating functions correspond to the right-hand side terms of (6) and (9). E_T and E_r can be written as (Adem, 1962):

$$E_T = -E(T) - E(T_s) + E(T_r) + \varepsilon[\sigma T_r^4 - E(T_r)] - 2\varepsilon[\sigma T_c^4 - E(T_c)] + (\alpha_2 + \alpha_3)I_d \quad (30)$$

$$E_r = -\sigma T_r^4 + E(T_s) + \varepsilon[\sigma T_c^4 - E(T_c)] + \alpha_1 I_d \quad (31)$$

The energy fluxes $E(T^*)$ are the fluxes emitted (or absorbed) by an atmospheric layer at temperature T^*; ε is the cloud cover fraction and T_c is its temperature; $\sigma = 5.6704\times10^{-8}$ Wm^{-2} K^{-4} is the Stefan-Boltzmann constant, and α_1, α_2 and α_3 are the fractional absorptions of insolation (I_d) by the surface of regolith, the gases of the atmosphere (mainly water vapor) and clouds, respectively. In the derivation of (27) and (28), it is assumed that, for long wave radiation, the surface and cloud cover emit as black bodies, but the atmosphere emits only a fraction of the black body emission (Adem, 1962):

$$E(T^*) = \epsilon_a \sigma T^{*4} \quad (32)$$

where ϵ_a is the atmospheric emissivity. For Mars, considering only the CO_2 emissivity, ϵ_a is equal to the hatched area in Figure 2 divided by the total area under the spectral black body curve. Also, dust, water vapor and ice have important infrared absorptions, with the main dust absorption band 1300-800 cm^{-1} (7.9 – 12.5 μm) centered at 1075 cm^{-1} (~ 9 μm) and can contribute with ~ 0.1 to ϵ_a in high dust concentration conditions (Ruff and Christensen, 2002). Then in accordance with (27), we express ϵ_a as:

$$\epsilon_a = \epsilon_{CO_2} + 0.06 + 0.04\cos(Ls + 80^o) \quad (33)$$

where ϵ_{CO_2} is the CO_2 atmospheric emissivity. The other right-hand side terms are the dust and water vapor and ice contributions, where we have neglected the overlap of the dust and 15 μm CO_2 bands.

The fraction α_1 can be found from (Adem, 1964):

$$\alpha_1 I_d = I_{Tot}[1 - (1 - k)\varepsilon](1 - \alpha) \quad (34)$$

where k is a function of the latitude and α is the surface albedo. Adem (1964) also supposes that $\alpha_2 = a_2$ and $\alpha_3 = b_3\,\varepsilon$, being a_2 and b_3 functions of the latitude and season.

From (5) and (13) the temperatures T_s and T can be expressed in terms of T_m, namely:

$$T_s = T_m + \Gamma/2\,(H - H_s)$$
$$T = T_m + \Gamma/2\,(H - H_s) \quad (35)$$

T_{s0} and T_{m0} are found from (1), using T_0 instead of T and taking the reference values $z = 0$ and $z = H/2$, such that $T_{s0} = (T^*)_{z=0} = T_0 + \Gamma H$ and $T_{m0} = (T^*)_{z=H/2} = T_0 + \Gamma H/2$. For the Earth we have the values of T_0, Γ and H for a standard atmosphere; with them we find T_{s0} and T_{m0}. For Mars we have $T_{s0} = 214.6K$, $\Gamma = 1.23$ Kkm^{-1} and $H = H_0 = 55$km, therefore $T_0 = T_{s0} - \Gamma H = 147K$ and $T_{m0} = T_{s0} - \Gamma H/2 = 180.8K$. Subtracting T_{s0}, T_{m0} and T_0 in (35):

$$T_s' = T_m' - \Gamma/2\,H_s$$
$$T' = T_m' + \Gamma/2\,H_s \quad (36)$$

For Earth (6) is linear and implicitly integrated over time, and it is convenient for us to assume mathematically that E_T and E_r are linear functions of T'_m and T'_r, represented by using Taylor series expansions; then with (36) and assuming that the cloud cover temperature is constant we have for the atmosphere, and from (30):

$$E_T = F_{30} + F'_{30}\,\varepsilon + F_{31}\,T'_m + (F_{32} + F'_{32}\,\varepsilon)\,T'_r + (\alpha_2 + \alpha_3) I_d \quad (37)$$

and for the surface, from (31):

$$E_r = F_{34} + F'_{34}\,\varepsilon + F_{35}\,T'_m + F_{36}\,T'_r + \alpha_1\,I_d \quad (38)$$

Except for dust, the Martian atmosphere is generally clear, although clouds of both water and CO_2 ice can form in certain regions and at certain times of the year. These clouds are not as dense or abundant as those on Earth, but they can reach a significant opacity. Water ice clouds in the equatorial belt are prominent during the aphelion in the boreal summer, and CO_2 ice clouds over the polar ice caps in winter (Read and Lewis, 2004). Therefore, clouds albedo would need to be considered and especially its greenhouse effect, because they are thin ice clouds. However, we neglected their radiative effect (shortwave and longwave) in (30), (31), (34), (37) and (38).

The coefficients F_n (n = 30….36) in (37) and (38) are:

$$F_{34} = -[E(T_0) + E(T_{s0}) - E(T_{r0})]$$

$$F'_{34} = -2F(T_C) + F(T_{r0})$$

$$F_{31} = \left(\frac{\partial F}{\partial T^*}\right)_{T_0} - 4\sigma T_0^3 + \left(\frac{\partial F}{\partial T^*}\right)_{T_{s0}} - 4\sigma T_{s0}^3$$

$$F_{32} = 4\sigma T_{r0}^3 - \left(\frac{\partial F}{\partial T^*}\right)_{T_{r0}}$$

$$F'_{32} = \left(\frac{\partial F}{\partial T^*}\right)_{T_{r0}}$$

$$F_{34} = -\sigma T_{r0}^4 + E(T_{s0})$$

$$F'_{34} = F(T_C)$$

$$F_{35} = 4\sigma T_{s0}^3 - \left(\frac{\partial F}{\partial T^*}\right)_{T_{s0}}$$

$$F_{35} = -4\sigma T_{r0}^3$$

Here we neglected the orographic effect in F_{30} and F_{34} because 2 $(\Gamma H_s/\mathrm{T}_0)E(\mathrm{T}_0)$ is ~ 8% of $E(T_0)$ and $2(\Gamma H_s/T_{s0})E(T_{s0})$ is ~ 6% of $E(T_{s0})$ for a typical value of $|H_s| = 6$ km. The function F(T^*) correspond to the atmospheric radiation window (non-hatched area in Figure 2), which is given by:

$$F(T^*) = (1 - \epsilon_a)\sigma T^{*4} \quad (39)$$

Assuming that the atmospheric emissivity is roughly independent of temperature:

$$\frac{\partial F}{\partial T^*} = (1 - \epsilon_a) 4\sigma T^{*3} \quad (40)$$

The turbulent vertical sensible heat flux is:

$$G_2 = c_H\,\rho_s\,c_p\,|V_s|(T_r - T_s) \quad (41)$$

where $c_H = 1.2\times10^{-3}$ is the constant heat transfer coefficient, $\rho_s = p_s/RT_s$ is the atmospheric density at the surface, $c_p = 815\ Jkg^{-1}\ K^{-1}$ is the specific heat at constant pressure and $|V_s|$ is the surface wind speed with a typical value of 6 ms^{-1}. Using (36) in (41):

$$G_2 = c_H\,\rho_s\,c_p\,|V_s|(T'_r - T'_m) + G_0 \quad (42)$$

where $G_0 = c_H\,\rho_s\,c_p\,|V_s|(T_{r0} - \tilde{T}_{s0})$, and $\tilde{T}_{s0} = T_{s0} + \Gamma H_s/2 \approx \mathrm{T}_{s0}$ because $\Gamma H_s/2$ is ~ 2% of T_{s0} for a typical value of $|H_s| = 6$ km.

G_1 is given by:

$$G_1 = \frac{k_v}{h_r}(T'_g - T'_r) \quad (43)$$

where $T'_g = T_g - T_{g0}$. We suppose that T_{g0} is equal to T_{r0}. T_g, which is computed from (10), is the temperature of the layer below the superficial layer.

2.7 Polar thermal energy balance

The main Martian condensation and sublimation processes are those of the CO_2 and they are mostly carried out at the poles. Then T'_m and T'_r will be calculated assuming that in (6) and (9) G_5 and G_3 are zero. At the poles, the CO_2 condensation starts at nightfall when the regolith temperature T_r descends below the CO_2 condensation (or saturation) temperature T_{sat}. The liberated latent heat increases T_r up to T_{sat}, which is a function of the atmospheric pressure (Pollack et al., 1981), given by:

$$T_{sat} = 149.2 + 6.48 \ln (0.00135\, p_s) \quad (44)$$

where p_s is given in hPa.

As the condensation can occur in the atmosphere as well as at the surface, the thermal energy balance is considered in a column including the surface and the atmosphere. Then we must use (6) and (9) together to find the net condensation rate given by $G_5 - G_3$. Therefore, considering that in (9) the term ST_r has been neglected, then adding (6) and (9), we obtain the rate of change (kg m^{-2} s^{-1}) of condensed mass m_c:

$$L \frac{\partial m_c}{\partial t} = G_5 - G_3 = -(E_T + E_r) - G_1 + ST - TU \quad (45)$$

where L is the sublimation latent heat.

Also, to obtain a better result for m_c, we will use in (45) the non-linear equations (30) and (31) instead of the linear equations (37) and (38). Then, considering that on the surface ice is in thermal equilibrium with its vapor (CO_2 gas) pressure, T_r is equal to T_{sat}; therefore, using (43) with $T_r = T_{sat}$, (45) can be expressed as:

$$L \frac{\partial m_c}{\partial t} = (1 - \epsilon_a)\sigma T_{sat}^4 + \epsilon_a \sigma T^4 - (1 - \alpha_p)\, I_d - k_v/h_r\, (T_g - T_{sat}) + ST - TU \quad (46)$$

where $\alpha_p = 1 - (\alpha_1 + \alpha_2 + \alpha_3)$ is the planetary albedo, and ST and TU are defined by (6). The first right-hand term is the main contributor to the formation of the ice layer, due to outgoing long-wave radiation from the surface through the window $(1 - \epsilon_a)$ in a cloud-free atmosphere, a process similar to the formation of a large scale radiative frost, occurring mainly during the polar night when $I_d = 0$ (this process can be attenuated by the greenhouse effect due to the presence of some CO_2 ice clouds over the polar caps during the season cold; see Read and Lewis [2004]). The second term has a smaller contribution and corresponds to long wave radiation emitted toward space, at the top of the atmosphere ($z = H$), by atmospheric CO_2 and dust. The third term contributes to the ice layer sublimation due to solar radiation after the end of the polar night. The fourth term also contributes to the ice sublimation provided $T_g > T_{sat}$, which happens even during the polar night, and this term modulates the CO_2 condensation. The fifth term corresponds to the thermal energy stored in the atmosphere by condensation. And the last term corresponds to the sublimation due to the horizontal turbulent heat transport at mid-latitudes.

In order to calculate T_{sat}, the p_s in (44) is determined by using (12) at $z = 0$, where the pressure is the global mean pressure gM_{CO_2}/A_M, where A_M is the Martian surface area and M_{CO_2} is the CO_2 atmospheric mass, which is equal to the CO_2 total available mass (considered constant) minus the condensed mass found from the integral of m_c over all the surface area covered by the ice. Then the atmospheric pressure p_s at any place on the surface, considering a mostly CO_2 atmosphere is:

$$p_s = \frac{gM_{CO_2}}{A_M} \left(\frac{T_s}{T_s + \Gamma H_s} \right)^{g/g\Gamma} \quad (47)$$

Equation (47) assumes that even though M_{CO_2} changes day by day, it is rapidly homogenized in all the planet; therefore, the reference pressure (at z=0) is considered uniform throughout. Then (47) shows that the surface pressure depends directly on the CO_2 atmospheric mass modulated by the potential relationship of temperatures: $[T_s/\ (T_s + \Gamma H_s)]^{g/R\Gamma}$. In (47) the first factor is global and provides the global pressure variation, the second one gives the local thermal-orographic effect, which according to (35) is a function of T_m, Γ and mainly H_s. The topography H_s was obtained from the Mars Orbiter Laser Altimeter (MOLA) on the Mars Global Surveyor (Smith et al., 1999a).

In (46) we calculated $(1 - \alpha_p)\ I_d$ assuming that α_2 and α_3 are negligible, considering only α_1. Then, neglecting clouds in (34):

$$(1 - \alpha_p) I_d = (1 - \alpha)\ I_{Tot} \quad (48)$$

where α is determined from https://www.mars.asu.edu/data/irtm_albedo/ and corresponds to the surface Lambertian albedo measured during a time of relatively clear atmosphere by the infrared thermal mapper (IRTM) on the Viking mission (Christensen, 1988). Equation (48) indicates that the planetary albedo, given by $\alpha_p = 1 - (1 - \alpha)\ I_{Tot}/I_d$ for $I_d > 0$, is a function of the surface albedo and the atmospheric dust, which reduces the solar radiation from I_d to I_{Tot}, increasing the planetary albedo. The atmospheric CO_2 that is condensed on the polar surface regions can have a relatively high albedo in visible wavelengths. If the ice is free of dust its albedo will

depend on the size of the ice grain varying between ~ 0.8, 0.6 and 0.4 for radii of 0.1, 0.5 and 2.0 mm, respectively. The albedo can be much reduced due to contamination with dust, and then in the model we used an albedo of 0.7 for the seasonal ice in the polar regions (Warren et al., 1990).

2.8 Solution of the model equations

The basic model variables are T'_m, T'_r and T'_g, calculated using the coupled equations (6), (9) and (10). Equations (6) and (9) are integrated implicitly. Following Adem (1965), in (9) the storage term ST_r is negligible in comparison with the other terms. Using finite differences in time for the storage atmospheric term ST, if T'_{mp} is the temperature in the previous time step, whose size is Δt, this term can be expressed as $c_1\,(T'_m - T'_{mp})/\Delta t$ and because the heating functions E_T, E_r, G_2 and G_1 are linear, (9) becomes a linear and algebraic equation, where T'_r is a linear function of T'_m and T'_g, then substituting T'_r in (6), we obtained a differential elliptic linear equation:

$$K\left[\frac{\partial^2 T'_m}{\partial\varphi^2} - \tan\varphi\,\frac{\partial T'_m}{\partial\varphi} + \frac{1}{co^2\,\varphi}\,\frac{\partial^2 T'_m}{\partial\psi^2}\right] - F_1\,T'_m = F_2 \qquad (49)$$

where F_1 and F_2 are functions of space and time determined as explained above (see also Adem, 1965). In particular, F_2 depends on the solar radiation fractions absorbed by the surface, atmosphere and clouds, and of the temperature T'_g. This temperature in turn is a function of the surface thermal inertia, which is important for the external atmospheric forcing. In fact, the temperature T'_m adjusts in such a way that (49) is fulfilled. Equation (49) is solved by finite differences using the Liebmann method, over a grid with a 1º × 1º resolution (the poles are not part of this grid). The boundary conditions are obtained from (49) in each of the two parallels nearest to the poles and are found assuming that the horizontal turbulent transport is zero close to the poles. Then, taking $K = 0$, the boundary condition is $T'_m = -F_1 / F_2$. According to Adem (1962), this solution differs significantly from observation in the polar regions of the Earth. However, it allows to determine a boundary condition close to the poles where the solution in spherical coordinates becomes indeterminate. Later we will see that the solution of (49) with this boundary condition is adequate in the polar regions, except in the Southern Hemisphere during autumn and winter. This boundary condition is also used as the first guess in the Liebmann method to determine the final solution for all the other grid points.

In order to solve (49), where Δt is a sol, we require first to know T'_g in (43), which is found by solving (10). Leighton and Murray (1966), using a very simplified thermal model, solved (10) using a resolution of 19 layers: nine equal layers of 1.5 cm and below them 10 equal layers 30 cm thick. Their choice of layers and layer thicknesses has the disadvantage of producing a temperature profile with discontinuity in the spatial derivative between the two layers of different thickness. To integrate (10), we use 24-time steps of 1.025 h to complete one sol. The soil is divided in 40 vertical layers including the surface, which have a variable thickness given by $\Delta z = h_r \exp[0.1(k - 1)]$, with $k = 1,2,\ldots,40$, in such a way that for the first 20 layers the thickness increases from 0and in the following 20 layers it increases from 0.15 to ~ 1 m, to finish with a total thickness of ~ 10.2 m. The boundary conditions for (10) are $(T_r^*)_{z1} = T_r$ and $(\partial T_r^* / \partial z)_{z40}$, here z_1 and z_{40} are the first and last middle level layer depths. Knowing T'_m from (49) and T'_g, considering (9) and that T'_r is a linear function of T'_m and T'_g, then T'_r is determined. Having T'_m, T'_g and T'_r, and if the condition $T_r = T'_r + T_{r0} \le T_{sat}$ is fulfilled, the change rate of condensed mass m_c can be found from (46). We have found that the best planetary value for the constants T_{r0} and T_{g0} is $T_{r0} = T_{g0} = 190$ K. With such values the linear and nonlinear solutions of (9) coincide. However, the consideration that E_T and E_r as linear functions (37, 38) of T'_m and T'_r, implies that during the polar night T_r is ~ 6 Cº higher than T_{sat}; and the condition to apply (46) must change to $T_r = T'_r + T_{r0} - 6\text{ K} \le T_{sat}$. We ran the model for several years until the seasonal cycles of T_m, T_r, T_g and p_s did not change from one year to the next, which occurs between years six and seven. We found that the greater the CO_2 total available mass, the more years of running are required to achieve the stability of the seasonal cycle. As a starting point for running the model, we use the representative surface value of –64 ºC for $p_s = 6.4$ mb. This value is just a reasonable guess to reach the Mars climatology.

The adjusted model parameters are the north and south polar thermal inertia and the total available CO_2 mass. We performed this adjustment in such a way that the calculated surface atmospheric pressure is as close as possible to the measured pressure by the Viking Lander 1 (VL1) at 22.3º N, 47.9º W and Viking Lander 2 (VL2) at 47.7º N, 225.7º W, and at the same time the calculated maximum condensed mass of south polar ice is closest to that estimated by Hess et al. (1979, 1980), from ~ 7.9 to 8.1×10^{15} kg. Examination of the maps of thermal inertia (Mellon et al., 2000) suggested to us a roughly linear trend of thermal inertia with latitude, where we set $I_T = 270$ J m^{-2} s$^{1/2}$ K for $\varphi = 89.5º$ (north polar cap) and $I_T = 165$ J m^{-2} s$^{1/2}$ K for $\varphi = -89.5º$ (south polar cap). These values are within the planetary scale range given by Jakosky (1986): 41.84 to 628 J m^{-2} s$^{1/2}$ K. For the total available CO_2 mass we found 2.72×10^{16} kg, while Paige and Wood (1992) and Smith et al. (1999b) found 3.04×10^{16} kg and ~ 3.2×10^{16} kg, respectively; Smith et al. (1999b) using this last value found ~ 1.1×10^{16} Kg for the mass of the south polar cap at $L_s = 150º$.

3. Results

Figure 5 shows, at the beginning of each boreal season (Ls = 0º [spring], Ls = 90º [summer], Ls = 180º [autumn] and Ls = 270º [winter]), the vertical profile of the regolith temperature computed using (10), corresponding to the VL1 (Fig. 5a) and VL2 (Fig. 5b) sites, and the central part (42.4 ºS, 298.5 ºW) of the Hellas Planitia (HPL) (Fig. 5c). We selected the HPL site because it is in the SH and is the deepest place in Mars (8.2 km below the surface reference level of 6.4 mb). The significant depth of penetration from the surface of the seasonal thermal wave is given by the e-folding length scale $(\tau_0\ k_v/\rho_r\ c_r\ \pi)^{1/2}$ (Read and Lewis, 2004); here, τ_0 is the period of the surface thermal signal; then for $\tau_0 = 5.94 \times 10^7$ s (one solar year), the depth for each of the three sites is 0.80, 0.85 and 0.67 m, respective-

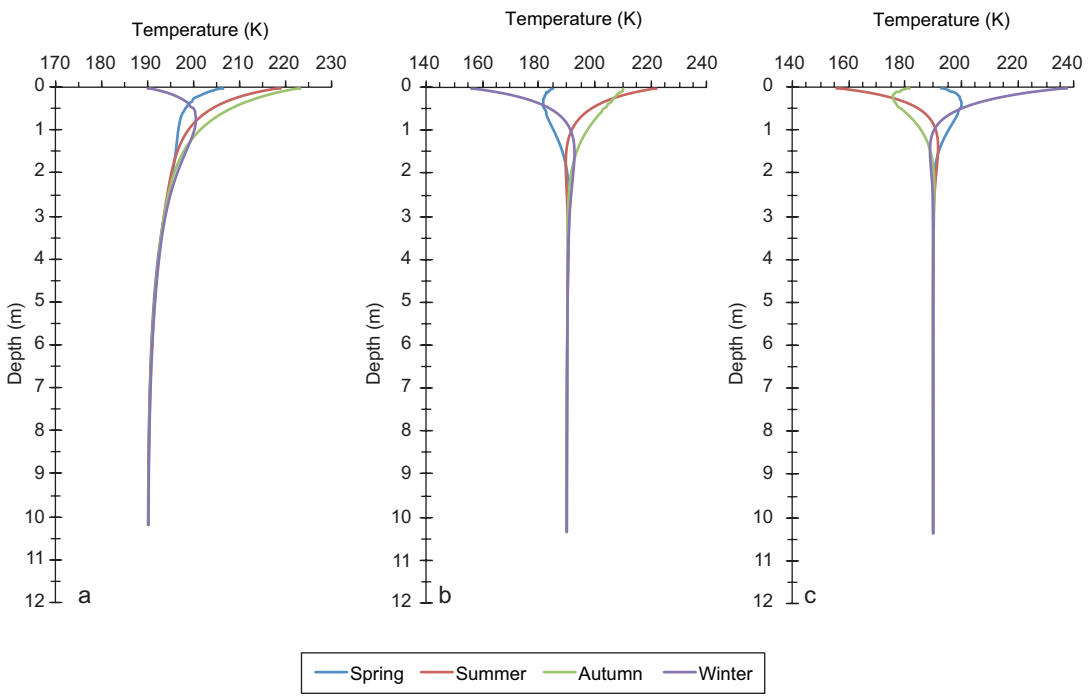

Fig. 5. Vertical temperature profiles of the Martian regolith at the beginning of each boreal season: *Ls* = 0º (spring), *Ls* = 90º (summer), *Ls* = 180º (autumn) and *Ls* = 270º (winter), at the sites of (a) Viking Lander 1 (VL1), (b) Viking Lander 2 (VL2), and (c) central Hellas Planitia region. The thermal wave is located between the surface and 1 m depth.

ly. In the diurnal cycle (which is not considered in our model), $\tau_0 = 8.64 \times 10^4$ s; then the penetration depth of its thermal wave is ~ 0.03 m, which is not significant for the time scales being examined here. Therefore, the seasonal regulation of the surface regolith temperature is achieved through the thermal conduction from the surface during the warm season, when the thermal wave can penetrate ~ 80 cm, and then this stored energy is returned to the surface during the cold season through the term G_1 in (9). In (45) or (46), G_1 contributes to moderate the CO_2 condensation during the polar night. In HPL during its warm season (boreal winter) heat is transmitted from the surface, with a temperature higher than 240 K (Fig. 5c), to the subsurface layers, from where it is transmitted back to the surface during its cold season (boreal summer).

The atmospheric temperature at any pressure level is found from (12); in particular at level $p_s/2$, the temperature is:

$$(T^*)_{p_s/2} = T_s\left(\frac{1}{2}\right)^{R\Gamma/g} \tag{50}$$

The temperature (in K) zonally averaged as a function of the latitude appears in Figure 6 for the four yearly seasons. The solid curves correspond to the temperature determined from (50) and the squares are the corresponding seasonal and vertical averages, obtained from the observed temperature profiles by the Mars Global Surveyor during six years (Hinson, 2008). The most important point from this figure is that temperatures between 140 and 160 K are found in the South Pole during spring and summer, and in autumn and winter in the North Pole, which shows

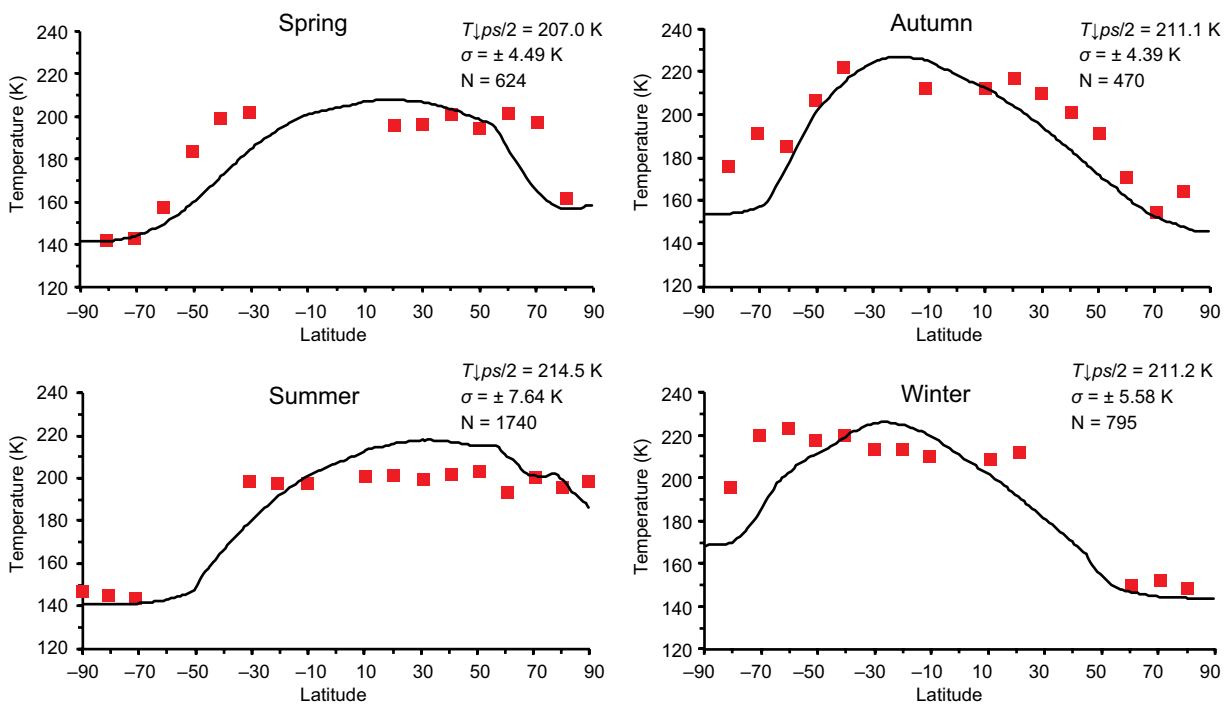

Fig. 6. Seasonal atmospheric temperature (K) at the level $p_s/2$ zonally averaged as a function of latitude. The curves are calculated from Eq. (50). The squares are the seasonal and vertical averages over a six-year period from the observed temperature profiles by the Mars Global Surveyor (Hinson, 2008). The seasonal average is calculated along the number of days corresponding to full 90º of L_S. To estimate a representative variability of the seasonal averages shown in red squares, we calculate the standard deviation with only the data from the tropical belt (30º N-30º S) because they are the most systematic (observations are scarce at extratropical and high latitudes) and cover practically the surface of half the planet. The average temperature ($T_{p_s/2}$), standard deviation (σ) and number of data (N) in the tropical belt are also shown in this figure.

some agreement with the observations. The agreement is rough considering that the Hinson (2008) values have low temperature resolution. We would like to point out that, when we used a CO_2 emissivity of 0.22 (instead of 0.24), we found an atmospheric average temperature decrease at the $p_s/2$ level of 1.1 K for spring, 1.1 K for summer, 1.2 K for autumn and 1.3 K for winter, supporting our claim that the difference in the band width can be considered negligible as discussed in the last paragraph of subsection 2.3 Atmospheric radiation. In Figure 6, we do not include the temperature curves for the case of the 0.22 emissivity because they are not appreciably different from those of 0.24 emissivity.

Figure 7 shows the seasonal variation of atmospheric pressure (in mb) at the surface ($z = H_s$), as a function of L_s, corresponding to the sites of VL1 (Fig. 7a), VL2 (Fig. 7b) and the central part of HPL (Fig. 7c). The solid curves correspond to the calculated pressure using (47), and the dots in Figure 7a and 7b, correspond, respectively, to average daily values observed over a period of four years for the VL1 and three years for the VL2 (Tillman, 1989). In Figure 7c, our estimate in HPL is compared with the daily average values (dotted curve) obtained from the reanalysis results of general circulation models described by Forget et al. (1999) and Millour et al. (2018), which constitute the MCD. Furthermore, from the surface pressure map of Toigo et al. (2013), obtained from CO_2 retrievals during the period L_s = 0º – 30º, we estimated a surface pressure value for the HPL of ~ 11 mb, that is also in agreement with Figure 7c. The observed seasonal variations of the surface pressure are mainly caused by the CO_2 sublimation and condensation processes at the poles. When sublimation of the south polar cap starts (starting at L_s =158º and ending around L_s = 280º, see Fig. 8), mainly due to solar heating, atmospheric pressure undergoes its maximum increase from ~ 6.8 to ~ 8.9 mb at the VL1 site, and from ~ 7.5 to ~ 9.8 mb at the VL2 site. This corresponds to a CO_2 exchange of ~ 8.1 $\times 10^{15}$ kg from the cap to the atmosphere (Hess et al., 1980). On comparing our calculated pressure change to observation, we notice that for the VL1 the model simulates such change with a phase delay of ~ 12º. For both VL1 and VL2, the observed pressure increases due to sublimation (between L_s = 0º and ~ 70º) of the north polar cap are only ~ 0.3 mb, much smaller than for the south polar cap. The calculated increase for both sites is ~ 0.8 mb, larger than the observations. Our results for VL1 and VL2 are comparable to those obtained by Wood and Paige (1992) with an energy balance model; however, in the case of VL1 they get a good

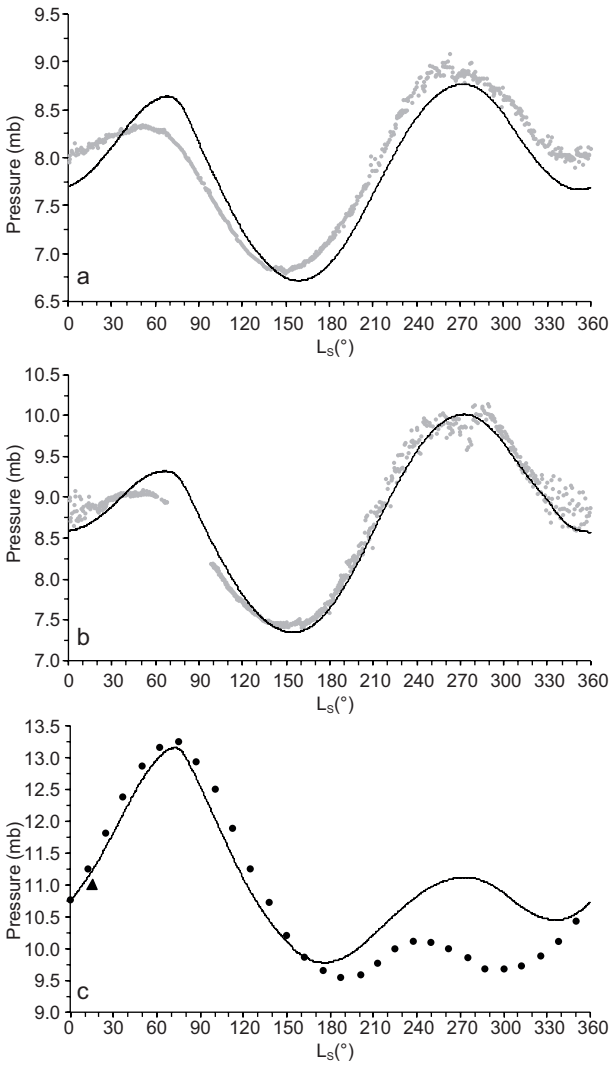

Fig. 7. Pressure (mb) at the surface ($z = H_s$) as a function of at the sites of Viking Lander 1 (VL1), (b) Viking Lander 2 (VL2), and (c) central Hellas Planitia region. The curves are calculated from Eq. (47), the dots in (a) and squares in (b) correspond to the average daily values observed over a four-year period (VL1) and three-year period (VL2). The dots in (c) are the daily average values obtained from reanalysis of the Mars Data Base and the triangle corresponds to the pressure of ~ 11 mb, estimated from the surface pressure map of Toigo et al. (2013) obtained from CO_2 retrievals during the period L_s = 0º-30º.

agreement with the observations without phase delay. At HPL the first pressure maximum (at $L_s = 75º$) is considerably larger than the second maximum (at $L_s = 275º$). Such difference with respect to the VL1 and VL2 sites is caused by the pressure change, because it is ruled by the CO_2 phase changes and by the potential relationship of temperatures (local thermo-orographic effect) shown in Figure 9. In this case, in the first maximum pressure, the factor due to the local orographic effect is 2.15, while in the second maximum this factor is 1.83. In other words, in HPL the local effect strongly modulates the pressure because ΓH_s is large and negative (see 47). In this figure, HPL (solid curve), at the SH, the maximum (at $L_s = 90º$) precedes the minimum (at $L_s = 270º$), opposite to VL1 (dot-dashed curve) and VL2 (dashed curve) at the NH.

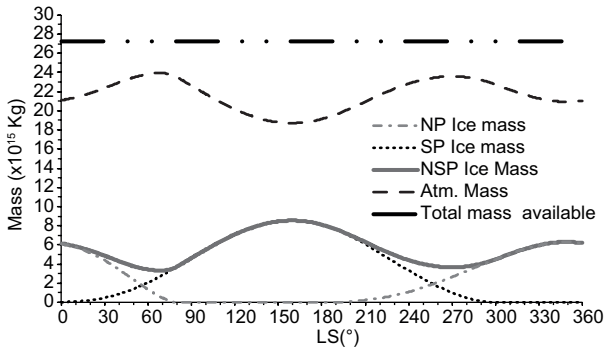

Fig. 8. Mass balance (10^{15} kg) as a function of L_s of the north polar ice cap (dot/dashed curve), the south polar ice cap (dotted curve) and the total mass of surface ice (solid curve). Also shown are the CO_2 atmospheric mass (dashed curve) and the total CO_2 available mass (double dotted/dashed curve) considered constant.

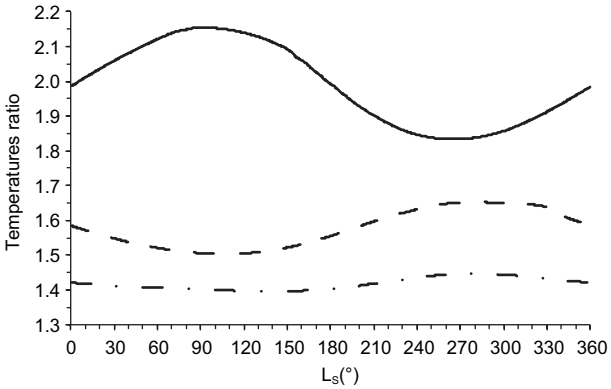

Fig. 9. Temperature ratio $[T_s/(T_s - \Gamma H_s)]^{g/R\Gamma}$ from Eq. (47) as a function of the areocentric longitude (L_s). The curves correspond to: Hellas Planitia region (solid), Viking Lander 1 (dashed) and Viking Lander 2 (dot/dashed).

The modeled CO_2 mass balance between the atmosphere and the polar caps is shown in Figure 8, presented as in Smith et al. (1999b). The south polar cap (dotted line) starts forming after the spring equinox, reaching its maximum in $L_s \sim 158º$ with 8.5×10^{15} kg, a value slightly greater to that estimated by Hess et al. (1980), 15% lower than that of Smith et al. (1999b) and 43% lower than that of Phillips et al. (2011). This polar cap forms layer by layer from the pole where it is thicker and reduces its thickness as the polar cap extends and reaches latitudes of 40º S, with a superficial density of 100 kg m^{-2} (Fig.10b); the growth dynamics is ruled by (46). The south polar cap starts decreasing from $L_s \sim 158º$ by sublimation and the increase of the daily average solar radiation (Fig. 3). After ~ 230 sols, at $L_s \sim 300º$, the polar cap has completely sublimated, but ~ 46 sols before $L_s \sim 190º$, the north polar cap starts forming (dot-dashed curve), reaching its maximum value of 6.3×10^{15} kg in ~ 263 sols (at $L_s \sim 350º$) and sublimates completely in 188 sols (at $L_s \sim 88º$). In this way, the planetary surface always keeps a minimum seasonal ice mass (solid curve) of 3.3×10^{15} kg. The CO_2 mass balance implies that the increment (decrement) of the surface total ice mass (solid curve), produces a decrement (increment) of the atmospheric CO_2 (dashed curve); then the total available CO_2 mass, which is the sum of the condensed and gas masses is a constant (double dot-dashed curve in Fig. 9). The growth of the north polar cap computed with (46) is also by layers (Fig. 10a) starting at the North Pole towards the south; however, this polar cap reaches a smaller extension and has a more circular structure than the south polar cap. The shape and extent of both ice caps simulated by the model, agree well with the shape and extent of seasonal frost on both poles, published by National Geographic (2016).

For polar temperatures about –127 ºC, the CO_2 ice density is ~ 1.6×10^3 kg m^{-3} (Hess et al., 1979), then a superficial layer of 100 kg m^{-2} is equivalent to a layer of 6.3 cm of thickness. Thereupon, in Figure 10, if curves of equal surface density are multiplied by a factor of 0.063, we find curves of equal ice thickness in centimeters. In this way, the thickness range of the

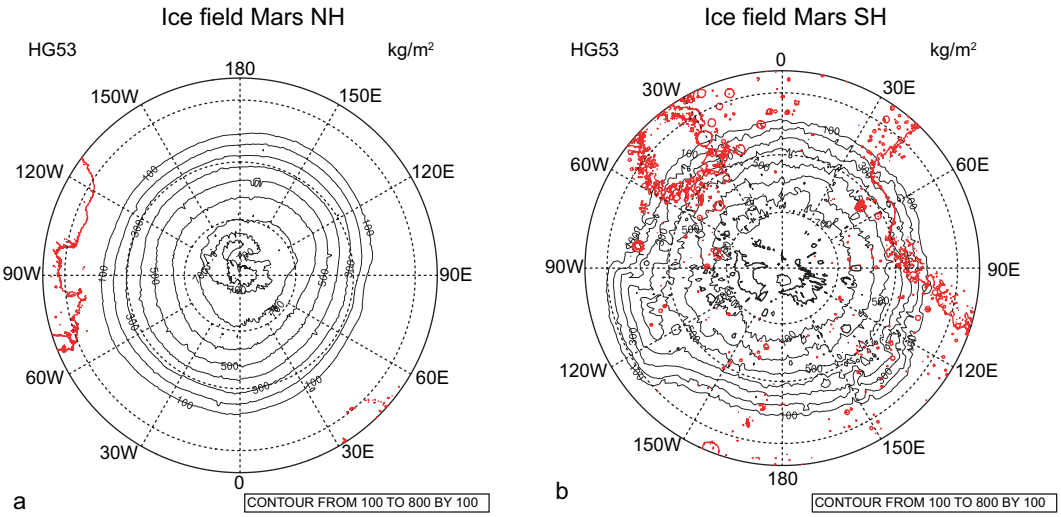

Fig. 10. Ice mass (kg m^{-2}), calculated from Eq. (46), at (a) North Pole for L_s = 342º (end of boreal winter) and (b) South Pole for L_s = 150º (end of boreal summer). The red contours indicate the reference level z = 0.

north and south polar caps is between 6.3 to 44.1 cm. Hess et al. (1979) estimated a south polar cap average thickness of 23 cm. Due to Kepler's Second Law, the south polar night (from L_s = 0º to L_s = 180°, Figs. 3 and 4) lasts 373 sols, which exceeds in 77 sols the north polar night (from L_s = 180º to L_s = 360º), which lasts 296 sols. This is one of the main reasons why the ice cap at the South Pole is more extensive and lasts longer than the North Pole cap, although the South Pole is ~ 4 km above the average reference level (~ 6.4 mb), which reduces the condensation temperature. In comparison, the North Pole is ~ 2 km below the reference level, which increases the condensation temperature, enabling the CO_2 condensation.

As mentioned above, the polar cap starts forming at the beginning of the polar night (hatched area in Fig. 3), reaching its maximum mass at the end of the polar night, resulting in a time delay between the polar mass evolution (Fig. 9, dotted curve for the South Pole and dot-dashed curve for the North) and the insolation (Fig. 3). From the right-hand side of (46), we notice that this maximum occurs when the sum of the third and fourth terms are equal to the sum of the first two terms, then $\partial m_c / \partial t = 0$. The cap's albedo (third term) and the regolith thermal conductivity (fourth term) produce the delay. That is to say, in relation to the third term, when the polar night ends ($I_d > 0$) the ice begins to reflect radiation, delaying its sublimation, and in relation to the fourth term, when the Sun begins to heat the surface, the lower layers of the regolith maintain a temperature less than the surface temperature (Fig. 5), so that $(T_g - T_{sat}) < 0$; therefore the fourth term, which is positive, represents a heat flow to the lower layers of the regolith so that it also has the effect of delaying the sublimation of ice.

4. Conclusions

1. Assuming a CO_2 atmosphere, we calculate its emission spectrum with E-Trans/HITRAN, resulting in the band of 15 mm (13.5-17 mm) and two large spectral transparent regions on both sides of it, through which the radiation emitted by the regolith and ice caps (considered as black bodies) goes toward space. We also include the atmospheric solar radiation extinction by dust and its longwave emission.

2. The thermodynamic equation establishes the energy balance between the absorbed solar radiation and the outgoing longwave radiation, incorporating also as heating mechanisms the latent heat released by CO_2 condensation, the sensible heat flux from the surface to the atmosphere, the latent heat flux due to the CO_2 ice sublimation, the heat exchange between the surface regolith layer and its lower layers, and the atmospheric planetary scale horizontal turbulent heat transport with an exchange coefficient of 3.7 ×

10^5 m^2 s^{-1}, which is an order of magnitude smaller than that employed in the terrestrial troposphere.

3. The regolith vertical temperature profile is explicitly determined using thermal inertia. The regolith surface layer temperature results from the balance of the net shortwave and longwave radiation, the thermal conduction from the lower regolith layers and the flux of sensible heat given to the atmosphere. The seasonal regulation of the surface regolith temperature is achieved through the thermal conduction from the surface during the warm season, when the thermal wave can penetrate ~ 80 cm, and then this stored energy is given back to the surface during the cold season. In this process the thermal inertia plays an important role because the e-folding length scale $(\tau_0 k_v/\rho_r c_r \pi)^{1/2} = (\tau_0/\pi)^{1/2}$ $I_T/\rho_r c_r$ is directly proportional to the thermal inertia and inversely proportional to the volumetric specific capacity ($\rho_r c_r$).

4. The Martian polar caps are formed by the atmospheric CO_2 condensation during the polar night in a process similar to that of a planetary scale frost, due to the outgoing infrared radiation emitted by the surface (which is assumed to emit as a black body), through the two transparent spectral regions mentioned in (1). Our model can predict the thickness and extent of polar ice caps and consequently the seasonal variation of atmospheric pressure on the surface, which agrees reasonably well at the sites of VL1 and VL2. In the Hellas Planitia case the model has a rough agreement with the MCD.

5. We found explicitly that the seasonal surface pressure variations are modulated by two factors: one associated with the global CO_2 mass Mars balance and the other due to the local thermal-orographic effect. The latter is manifested in the seasonal surface pressure cycle in the Hellas Planitia.

6. The thermodynamic model of Mars that we have developed here can be used in the future to simulate some physical processes that we did not consider in this work, such as the possible greenhouse effect of polar clouds, the climatic effect of the albedo of the polar cap modified by dust pollution, and the warming of the Martian atmosphere by the increase of some greenhouse gases such as CO_2 itself, which could be used to carry out the terraformation of Mars or the modelling of the solar minima, in order to assess their influence on the Mars climate.

Acknowledgements

This work was partially supported by the grant of PAPIIT-UNAM (IN102415). We thank to Alejandro Aguilar Sierra and Oscar Sánchez-Meneses for preparing the database and programs for the numerical computations. We acknowledge one anonymous referee for the very detailed revision and suggestions.

References

Adem J. 1962. On the theory of the general circulation of the atmosphere. Tellus 14, 102-115. https://doi.org/10.3402/tellusa.v14i1.9532

Adem J. 1963. Preliminary computations on the maintenance and prediction of seasonal temperatures in the troposphere. Monthly Weather Review 91, 376-386. https://doi.org/10.1175/1520-04931963.091<0375:PCOTMA>2.3.CO;2

Adem J. 1964. On the physical basis for the numerical prediction of monthly and seasonal temperatures in the troposphere-ocean-continent system. Monthly Weather Review 92, 91-104. https://doi.org/10.1175/1520-0493(1964)092<0091:OTPBFT>2.3.CO;2

Adem J. 1965. Experiments aiming at monthly and seasonal numerical weather prediction. Monthly Weather Review 93, 495-503. https://doi.org/10.1175/1520-0493(1965)093<0495:EAAMAS>2.3.CO;2

Adem J. 1981a. Numerical experiments on ice age climates. Climate Change 3, 155-171. https://doi.org/10.1007/BF00154434

Adem J. 1981b. Numerical simulation of the annual cycle of climate during the ice ages. Journal of Geophysical Research 86, 12015-12034. https://doi.org/ 10.1029/JC086iC12p12015

Adem J. 1982. Simulation of the annual cycle of climate with a thermodynamic numerical model. Geofísica Internacional 21, 229-247.

Adem J, Mendoza VM, Ruiz A, Villanueva EE, Garduño R. 2000. Recent numerical experiments on three-months extended and seasonal weather prediction with a thermodynamic model. Atmósfera 13, 53-83.

Appelbaum J, Landis GA, Sherman I. 1993. Solar radiation on Mars—Update 1991. Solar Energy 50, 35-51. https://doi.org/10.1016/0038-092X(93)90006-A

Barnes JR, Pollack JB, Haberle RM, Zurek RW, Leovy CB, Lee H, Schaeffer J. 1993. Mars atmospheric dynamics as simulated by the NASA/Ames general circulation model, 2. Transient baroclinic eddies. Journal of

Geophysical Research 98/(E2), 3125-3148. https://doi.org/10.1029/92JE02935

Christensen PR. 1988. Global albedo variations on Mars: Implications for active aeolian transposition, and erosion. Journal of Geophysical Research 93, 7611-7624. https://doi.org/10.1029 /JB093iB07p07611.

Defant A. 1921. Die Zirculation der Atmosphäre in den gemässigten Breitern der Erde, Geografike Annales 3, 209-266. https://doi.org/10.1080/20014422.1921.11880911

Fanale FP, Cannon WA. 1971. Adsorption on the Martian regolith. Nature 230, 502-504. https://doi.org/10.1038/230502a0

Fanale FP, Jakosky BM. 1982. Regolith-atmosphere exchanges of water and carbon dioxide on Mars. Effects on atmospheric history and climate change. Planetary and Space Science 30, 819-831. https://doi.org/10.1016/0032-0633(82)90114-3

Forget F, Hourdin F, Fournier R, Hourdin C, Talagrand O, Collins M, Lewis SR, Read PL, Huot J-P. 1999. Improved general circulation models of the Martian atmosphere from the surface to above 80 km. Journal of Geophysical Research 104, 24155-24176. https://doi.org/10.1029/1999JE001025

Franz HB, Trainer MG, Malespin CA, Mahaffy PR, Atreya SK, Becker RH, Benna M, Conrad PG, Eigenbrode JL. 2017. Initial SAM calibration gas experiments on Mars: Quadrupole mass spectrometer results and implications. Planetary and Space Science 138, 44-54. https://doi.org/10.1016/j.pss.2017.01.014

Hess SL, Henry RM, Tillman JE. 1979. The seasonal variation of atmospheric pressure on Mars as affected by the south polar cap. Journal of Geophysical Research 84, 2923-2927. https://doi.org/10.1029/JB084iB06p02923

Hess SL, Ryan JA, Tillman JE, Henry RM, Leovy CE. 1980. The annual cycle of pressure on Mars measured by Viking Landers 1 and 2. Geophysical Research Letters 7, 197-200. https://doi.org/10.1029/GL007i003p00197

Hinson DP (2008) Mars Global Surveyor radio occultation profiles of the neutral atmosphere—Reorganized. NASA Planetary Data System. Available at: http://pds-atmospheres.nmsu.edu/pdsd/archive/data/mgs-m-rss-5-tps-v10/mors_1101/

Holopainen EO. 1983. Transient eddies in mid-latitudes: Observation and interpretation. In: Large-scale dynamical processes in the atmosphere (Hoskins BJ, Pearce RP, Eds.). Academic Press, San Diego, CA, 201-233.

Jakosky BM. 1986. On the thermal properties of Martian fines. Icarus 66, 117-124. https://doi.org/10.1016/0019-1035(86)90011-4

Kondratyev KY. 1969. Radiation in the atmosphere. Academic Press, New York-London, 911 pp.

Leighton RB, Murray BC. 1966. Behavior of carbon dioxide and other volatiles on Mars. Science 153, 136-44. https://doi.org/10.1126/science.153.3732.136

McKay CP. 1999. Bringing life of Mars. In the future of space exploration. Scientific American Quarterly 10, 52-57.

Mellon MT, Jakosky BM, Kieffer HH, Christensen PR. 2000. High resolution thermal inertia mapping for the Mars Global Surveyor Thermal Emission Spectrometer. Icarus 148, 437-455. https://doi.org/10.1006/icar.2000.6503

Mendoza VM, Mendoza B, Garduño R, Adem J. 2010. Simulation of the surface temperature anomalies in the Northern Hemisphere during the last 300 years of the Little Ice Age using a thermodynamic model. Climate Research 43, 263-273. https://doi.org/10.3354/cr00938

Mendoza VM, Mendoza B, Garduño R, Villanueva EE, Adem J. 2016. Solar activity cloudiness effect on NH warming for 1980-2095. Advances in Space Research 57, 1373-1390. https://doi.org/10.1016/j.asr.2015.11.024

Mendoza VM, Villanueva EE, Garduño R, Sánchez-Meneses O. 2017. Atmospheric emissivity with clear sky computed by E-Trans/HITRAN. Atmospheric Environment 155, 174-188. https://doi.org/10.1016/j.atmosenv.2017.01.048

Milankovitch M. 1920. Théorie mathématique des phénomènes thermiques produits par la radiation solaire. Gauthier-Villars et Cie, Paris.

Millour E, Forget F, Spiga A, Vals M, Zakharov V, Montabone L, Lefèvre F, Montmessin F, Chaufray J-Y, López-Valverde MA 4, González-Galindo F, Lewis SR, Read PL, Desjean M-C, Cipriani F, the MCD development team. 2018. The Mars climate database (version 5.3). Scientific workshop From mars express to ExoMars, 27-28 February, ESAC, Madrid, Spain.

National Geographic. 2016. November Mars Issue, with 2 sided supplements: Colonizing Mars and Mars Map. Editor: Matthew W. Chwastyk, Text: Jeremy Berlin, Map edition: Gus Platis and Investigation: Taryn Salinas. NASA: Gazetter of Planetary Nomenclature. Planetary Geomagnetic Group. USGS: NASA/JPL: University of Arizona; Applied Physics Laboratory, Johns Hopkins University; Carnegie Institute: Rosalyn Hayward, James Skinner and Kenneth Tanaka. Astro-

geological Science Center. USGS. Copyright © 2016 National Geographic Partners, LLC Washington, D.C. Printed in October 2016.

Paige DA, Wood SE. 1992. Modeling the Martian seasonal CO2 cycle 2. Interannual variability. Icarus 99, 15-27. https://doi.org/10.1016/0019-1035(92)90167-6

Piqueux S, Christensen PR. 2011. Temperature-dependent thermal inertia of homogeneous Martian regolith. Journal of Geophysical Research 116, 1-18. https://doi.org/10.1029/2011JE003805

Pollack JB, Leovy CB, Greiman PW, Mintz Y. 1981. A Martian general circulation model experiment with large topography. Journal of the Atmospheric Sciences 38, 3-29. https://doi.org/10.1175/1520-0469(1981)038<0003:AMGCEW>2.0.CO;2

Pollack JB, Haberle RM, Schaeffer J, Lee H. 1990. Simulations of the general circulation of the Martian atmosphere 1: Polar processes. Journal of Geophysical Research 95, 1447-1473. https://doi.org/10.1029/JB095iB02p01447

Read PL, Lewis SR. 2004. The Martian climate revisited: Atmosphere and environment of a desert planet. Springer and Praxis, Chichester, UK, 326 pp. https://doi.org/10.5860/choice.42-0920

Phillips JR, Davis BJ, Tanaka KL, Byrne S, Mellon MT, Putzig NE, Haberle RM, Kahre MA, Campbell BA, Carter LM, Smith IB, Holt JW, Smrekar SE, Nunes DC, Plaut JJ, Egan AF, Titus TN, Seu R. 2011. Massive CO_2 ice deposits sequestered in the south polar layered deposits of Mars. Science 332, 838-841. https://doi.org/10.1126/science.1203091

Rothman LS, Jacquemart D, Barbe A, Chris Benner D, Birk M, Brown LR, Carleer MR, Chackerian C Jr, Chanse K, Coudert LH, Dana V, Devi VM, Flaud J-M, Gamache RR, Goldman A, Hartmann J-M, Jucks KW, Maki AG, Mandin J-Y, Massie ST, Orphal J, Perrin A, Rinsland CP, Smith MAH, Tennyson J, Tolchenov RN, Toth RA, Vander Auwera J, Varanasi P, Wagner G. 2005. The HITRAN 2004 molecular spectroscopic data base. Journal of Quantitative Spectroscopy and Radiative Transfer 96, 139-204. https://doi.org//10.1016/j.jqsrt.2004.10.008

Ruff S.W, Christensen PR. 2002. Bright and dark regions on Mars: Particle size and mineralogical characteristics based on Thermal Emission Spectrometer data. Journal of Geophysical Research 107, E12-5127. https://doi.org/10.1029/2001JE001580

Smith DE, Zuber MT, Solomon SC, Phillips RJ, Head JW, Garvin JB, W. Banerdt WB, Muhleman DO, Pettengill GH, Neumann GA, Lemoine FG, Abshire JB, Aharonson O, Brown CD, Hauck SA, Ivanov AB, McGovern PJ, Zwally HJ, Duxbury TC. 1999a. The global topography of Mars and implications for surface evolution. Science 284, 1495-1503. https://doi.org/10.1126/science.284.5419.1495

Smith DE, Zuber MT, Haberle RM, Rowlands DD, Murphy JR. 1999b. The Mars seasonal CO_2 cycle and the time variation of the gravity field: A general circulation model simulation. Journal of Geophysical Research 104, 1885-1896. https://doi.org/10.1029/1998JE900024

Spinrad HG, Münch LD, Kaplan D. 1963. The detection of water vapour on Mars. The Astrophysical Journal 137, 1319-1321.

Stephen RL, Collins M, Read PL, Forget F, Hourdin F, Fournier R, Hourdin C, Talagrand O, Huot J-P. 1999. A climate database for Mars. Journal of Geophysical Research-Planets 104, 24 177-24 194. https://doi.org/10.1029/1999JE001024

Stephen RL. 2003. Modelling the Martian atmosphere. Astronomy & Geophysics 44, 4.6-4.14 https://doi.org/10.1046/j.1468-4004.2003.44406.x

Stewart HJ. 1945. Kinematics and dynamics of flui flow. Handbook of meteorology. McGraw Hill, New York.

Tillman JE. 1989. Planetary data system, VL1/VL2 Mars Meteorology Data Calibrated Pressure Data VI.0, VL1/VL2-M-MET-3-PV1.0. Jet Propulsion Laboratory MS 301-275, Pasadena, CA.

Toigo AD, Richardson MI. 2000. Seasonal variation of aerosols in the Martian atmosphere. Journal of Geophysical Research 105, 4109-4121. https://doi.org/10.1029/1999JE001132

Toigo AD, Smith MD, Seelos FP, Murchie SL. 2013. High spatial and temporal resolution sampling of Martian gas abundances from CRISM spectra. Journal of Geophysical Research-Planets 118, 89-104. https://doi.org/10.1029/2012JE004147

Warren SG, Wiscombe WJ, Firestone JF. 1990. Spectral albedo and emissivity of CO_2 in Martian polar caps: Model results. Journal of Geophysical Research 95, 14717-14741. https://doi.org/10.1029/JB095iB09p14717

Withers P, Smith MD. 2006. Atmospheric entry profiles from the Mars Exploration Rovers Spirit and Opportunity. Icarus 185, 133-142. https://doi.org/10.1016/j.icarus.2006.06.013.

Wood SE, Paige DA. 1992. Modeling the Martian seasonal CO_2 cycle. Icarus 99, 1-14. https://doi.org/10.1016/0019-1035(92)90166-5

APPENDIX

List of symbols

$H = H_0$	Height of the atmospheric layer referred to the level $z = 0$, considered constant equal to H_0.
H_s	Orographic height relative to the planet's reference level of ~ 6.4 mb
T^*	Temperature (K) of the atmospheric layer.
$T = T_0 + T'$	Temperature at $z = H$, where T_0 is a constant and $T' << T_0$..
$T_m = T_{m0} + T'_m$	Temperature vertically averaged in the atmospheric layer, where T_{m0} is a constant and $T'_m << T_{m0}$.
$T_r = T_{r0} + T'_r$	Temperature of the surface regolith layer, where T_{r0} is a constant and $T'_r << T_{r0}$.
T_s	Surface temperature.
T_e	Equivalent temperature of CO_2.
$T^{*\prime\prime}$	Temperature perturbation field.
T_c	Temperature of the cloud cover fraction.
T_{s0}	Constant surface temperature for Mars.
T_{sat}	CO_2 temperature of saturation.
$T'_g = T_g - T_{g0}$	$T_{g0} = T_{r0}$; T_g is the temperature of the regolith layer below the superficial layer.
E_T	Shortwave and longwave net radiation in the atmosphere.
E_r	Shortwave and longwave net radiation in the surface of the regolith.
G_1	Thermal energy gained by the upper regolith layer by heat conduction from the lower layers.
G_2	Vertical turbulent sensible heat flux from the surface of the regolith to the atmosphere.
G_3	Thermal energy lost by the vertical turbulent latent heat flux by CO_2 ice sublimation.
G_5	Release of latent heat by the condensation.
F_n	Taylor series coefficients.
A_M	Martian surface area.
I_T	Thermal inertia.
I	Instantaneous solar radiation.
I_d	Average daily insolation.
I_{Tot}	Total solar radiation.
S_0	Total solar irradiance.
L	Sublimation latent heat .
L_s	Areocentric longitude.
L_s^p	Areocentric longitude at the perihelion.
$\|V_s\|$	Surface wind speed.
Γ	Constant lapse rate.
K	*Austauch* coefficient.
P	Duration of the sol.
p^*	Atmospheric pressure.
p_s	Pressure at surface.
p_e	Equivalent pressure of CO_2.
ρ^*	Density in the troposphere.
ρ_m	Layer average density.
ρ_r	Density of the regolith.
c_H	Constant heat transfer coefficient.
c_p	Specific heat at constant pressure.
c_r	Specific heat of the regolith.
c_V	Specific heat at constant volume.
h_r	Thickness of the regolith layer.

k_V	Thermal conductivity coefficient.
r_0	Mars radius.
r	Instantaneous Sun-Mars distance.
r_c	Molecular ideal gas weight.
ω	Hourly angle.
ω_1	Longitude at noon.
a_0	Orbit's major semiaxis.
η	Obliquity.
τ	Optical thickness.
τ_0	Period of the surface thermal signal.
$v^{*\prime\prime}$	Meridional component of the turbulence or eddy velocity.
ε	Cloud cover fraction.
σ	Stefan-Boltzman constant.
α_1	Fractional absorption of insolation by the surface of the regolith.
α_2	Fractional absorption of insolation by the gases in the atmosphere.
α_3	Fractional absorption of insolation by clouds.
α_p	Planetary albedo.
α_p	Atmospheric emissivity.
ϵ_{CO_2}	CO_2 atmospheric emissivity.
m_c	Condensed mass.
g	Gravity acceleration.
ϕ	Latitude in radians.
ψ	Longitude in radians.
z	Height measured from the surface.
Z	Zenith angle .
t	Time.